

Symmetric Parallax Attention for Stereo Image Super-Resolution

Yingqian Wang*, Xinyi Ying*, Longguang Wang, Jungang Yang[†], Wei An, Yulan Guo

Abstract—Although recent years have witnessed the great advances in stereo image super-resolution (SR), the beneficial information provided by binocular systems has not been fully used. Since stereo images are highly symmetric under epipolar constraint, in this paper, we improve the performance of stereo image SR by exploiting symmetry cues in stereo image pairs. Specifically, we propose a symmetric bi-directional parallax attention module (biPAM) and an inline occlusion handling scheme to effectively interact cross-view information. Then, we design a Siamese network equipped with a biPAM to super-resolve both sides of views in a highly symmetric manner. Finally, we design several illuminance-robust bilateral losses to enforce stereo consistency. Experiments on four public datasets have demonstrated the superiority of our method. As compared to PASSRnet, our method achieves notable performance improvements with a comparable model size. Source codes are available at <https://github.com/YingqianWang/iPASSR>.

Index Terms—Stereo image super-resolution, Parallax attention, Siamese network, Occlusion handling

I. INTRODUCTION

WITH recent advances in stereo vision, dual cameras are commonly adopted in mobile phones and autonomous vehicles. Using the complementary information (i.e., cross-view information) provided by binocular systems, the resolution of image pairs can be enhanced [1]–[6]. However, it is challenging to achieve good performance in stereo image super-resolution (SR) due to the following issues:

- *Varying parallax.* Objects at different depths have different disparity values and thus locate at different positions along the horizontal epipolar line. It is challenging to capture reliable stereo correspondence and effectively integrate cross-view information for stereo image SR.
- *Information incorporation.* Since context information within a single view (i.e., intra-view information) is crucial and contributes to stereo image SR in a different manner, it is important but challenging to fully incorporate both intra-view and cross-view information.
- *Occlusions & boundaries.* In occlusion and boundary areas, pixels in one view cannot find their correspondence in the other view. In this case, only intra-view information is available for stereo image SR. It is challenging to fully

This work was partially supported in part by the National Natural Science Foundation of China (Nos. 61972435, 61401474, 61921001).

Y. Wang, X. Ying, L. Wang, J. Yang, W. An, and Y. Guo are with the College of Electronic Science and Technology, National University of Defense Technology, P. R. China. Y. Guo is also with the School of Electronics and Communication Engineering, Sun Yat-sen University, P. R. China. Emails: {wangyingqian16, yingxinyi18, yangjungang, yulan.guo}@nudt.edu.cn.

*Y. Wang and X. Ying contribute equally to this work and are co-first authors. [†]Corresponding author: Jungang Yang.



Fig. 1: Visual results achieved by PASSRnet [2], [3], SRResNet+SAM [4], and our iPASSR network for 4×SR. These results are achieved on scene *Test_0002* of the Flickr1024 dataset [7]. Our method can recover more faithful and stereo-consistent details than other methods.

use cross-view information in non-occluded regions while maintaining promising performance in occluded regions.

Recently, several methods have been proposed to address the above issues. Wang et al. [2], [3] addressed the varying parallax issue by proposing a parallax attention module (PAM), and developed a PASSRnet for stereo image SR. Ying et al. [4] addressed the information incorporation issue by equipping several stereo attention modules (SAMs) to the pre-trained single image SR (SISR) networks. Song et al. [5] addressed the occlusion issue by checking stereo consistency using disparity maps regressed by parallax attention maps. Although continuous improvements have been achieved, the inherent correlation within stereo image pairs are still under exploited, which hinders the performance improvement of stereo image SR methods.

Since super-resolving left and right images are highly symmetric, the inherent correlation within an image pair can be fully used by exploiting its symmetry cues. In this paper, we improve the performance of stereo image SR by exploiting symmetries on three levels: 1) On the module level, we design a symmetric bi-directional parallax attention module (biPAM) to interact cross-view information. With our biPAM, occlusion maps can be generated and used as a guidance for cross-view feature fusion. 2) On the network level, we propose a Siamese network equipped with our biPAM to super-resolve both left and right images. Experimental results demonstrate that jointly super-resolving both sides of views can better exploit the correlation between stereo images and is contributive to SR performance. 3) On the optimization level, we exploit symmetry cues by designing several bilateral

losses. Our proposed losses can enforce stereo consistency and is robust to illuminance changes between stereo images. We perform extensive ablation studies to validate the effectiveness of our method. Comparative experiments on the KITTI 2012 [8], KITTI 2015 [9], Middlebury [10], and Flickr1024 [7] datasets have demonstrated the superiority of our method. As shown in Fig. 1, our method (namely, iPASSR) can recover more faithful and stereo-consistent details than several state-of-the-art SR methods.

This paper is an extension of our previous work *PASSRnet* [2], [3]. This work is different from *PASSRnet* in several aspects, as summarized below:

- We design a novel Siamese network to better exploit symmetry cues for stereo image SR. Different from *PASSRnet* [2], [3], the proposed network can super-resolve both sides of views within a single inference.
- We develop a symmetric and bi-directional parallax attention module. Compared to PAMs in [2], [3], our biPAM is more compact and can effectively handle occlusions.
- Experimental results demonstrate that our method achieves significant performance improvements over *PASSRnet* with a comparable model size.

The rest of this paper is organized as follows. In Section II, we briefly review the related work. In Section III, we introduce our proposed method including network architecture, occlusion handling scheme, and loss functions. Experimental results are presented in Section IV. Finally, we conclude this paper in Section V.

II. RELATED WORK

In this section, we briefly review several major works on single-image and multi-image SR.

A. Single image SR

SISR is a long-standing problem and has been investigated for decades. In recent years, deep learning-based SISR methods have achieved promising performance in terms of both reconstruction accuracy [11]–[15] and visual quality [16]–[18]. Dong et al. [19] proposed the first CNN-based SR network (i.e., SRCNN) to reconstruct high-resolution (HR) images from low-resolution (LR) inputs. Kim et al. [20] proposed a deeper network with 20 layers (i.e., VDSR) to improve SR performance. Afterwards, SR networks became increasingly deep and complex, and thus more powerful in intra-view information exploitation. Lim et al. [12] proposed an enhanced deep SR network (i.e., EDSR) using both local and residual connections. Zhang et al. [13] combined residual connection [21] with dense connection [22], and proposed residual dense network (i.e., RDN) to fully use hierarchical feature representations for image SR. More recently, the performance of SISR has been further improved by RCAN [14] and SAN [15].

B. Multi-image SR

As compared to SISR methods which exploit context information within only one view, multi-image SR methods aim at using the additional information provided by multiple images to improve SR performance.

1) *Video SR*: Liao et al. [23] proposed the first CNN-based video SR method by performing motion compensation and SR sequentially. Wang et al. [24], [25] improved this scheme by estimating optical flow in HR space. Tao et al. [26] proposed a joint learning framework for motion estimation and SR reconstruction. Recently, implicit motion compensation approaches (e.g., 3D convolution [27], [28], dynamic upsampling filter [29], and deformable convolution [30]–[32]) have been extensively studied for video SR to achieve promising performance.

2) *Light field image SR*: Compared to video frames, light field (LF) images are well-structured since the displacement among different views is highly related to their angular coordinates and depth values. Yoon et al. [33], [34] proposed the first LF image SR network (i.e., LFCNN). Wang et al. [35] developed a bi-directional recurrent CNN (i.e., LFNet) for LF image SR. Recently, several approaches including residual networks [36], 4D convolution [37], [38], deformable convolution [39], and spatial-angular interaction [40] were proposed to enhance the performance of LF image SR.

3) *Reference-based SR*: Reference-based SR (RefSR) aims at super-resolving an LR image using one (e.g., [41]–[44]) or multiple (e.g., [45], [46]) external HR images as reference. Yue et al. [45] proposed a RefSR method by retrieving similar reference images from web. Zheng et al. [41] proposed a CrossNet and used optical flow to align input and reference images. Subsequently, they proposed CrossNet++ [47] to tackle the RefSR problem with a significant resolution gap ($8\times$). Zhang et al. [42] proposed a SRNTT network to adaptively transfer the texture from reference images to the target image according to their textural similarity. Yang et al. [43] proposed a texture transformer network to attentively learn deep feature representation between target and reference images. More recently, Yan et al. [46] proposed a content-independent multi-reference SR method to adaptively match the visual pattern between reference and target images. Xie et al. [44] improved SRNTT [42] by using a task-specific feature extractor for feature matching and swapping and designed an end-to-end training framework for RefSR.

4) *Stereo image SR*: The disparities in stereo images are much larger than those in video frames and LF images, and the resolution of both left and right images is low. Consequently, video SR, LF image SR, and RefSR methods are all unsuitable for stereo image SR. To handle this problem, Jeon et al. [1] proposed the first network (i.e., StereoSR) to learn a parallax prior by jointly training two cascaded sub-networks. The cross-view information is integrated by concatenating the left image and a stack of right images with different pre-defined shifts. Wang et al. [2], [3] proposed a parallax attention module to model stereo correspondence with a global receptive field along the epipolar line. Ying et al. [4] proposed a stereo attention module and embedded it into pre-trained SISR networks for stereo image SR. Song et al. [5] combined self-attention with parallax attention to propose a SPAMnet for stereo image SR. Furthermore, stereo consistency was addressed by SPAMnet [5] using disparity maps regressed from parallax attention maps. More recently, Yan et al. [6] proposed a domain adaptive stereo SR network (DASSR).

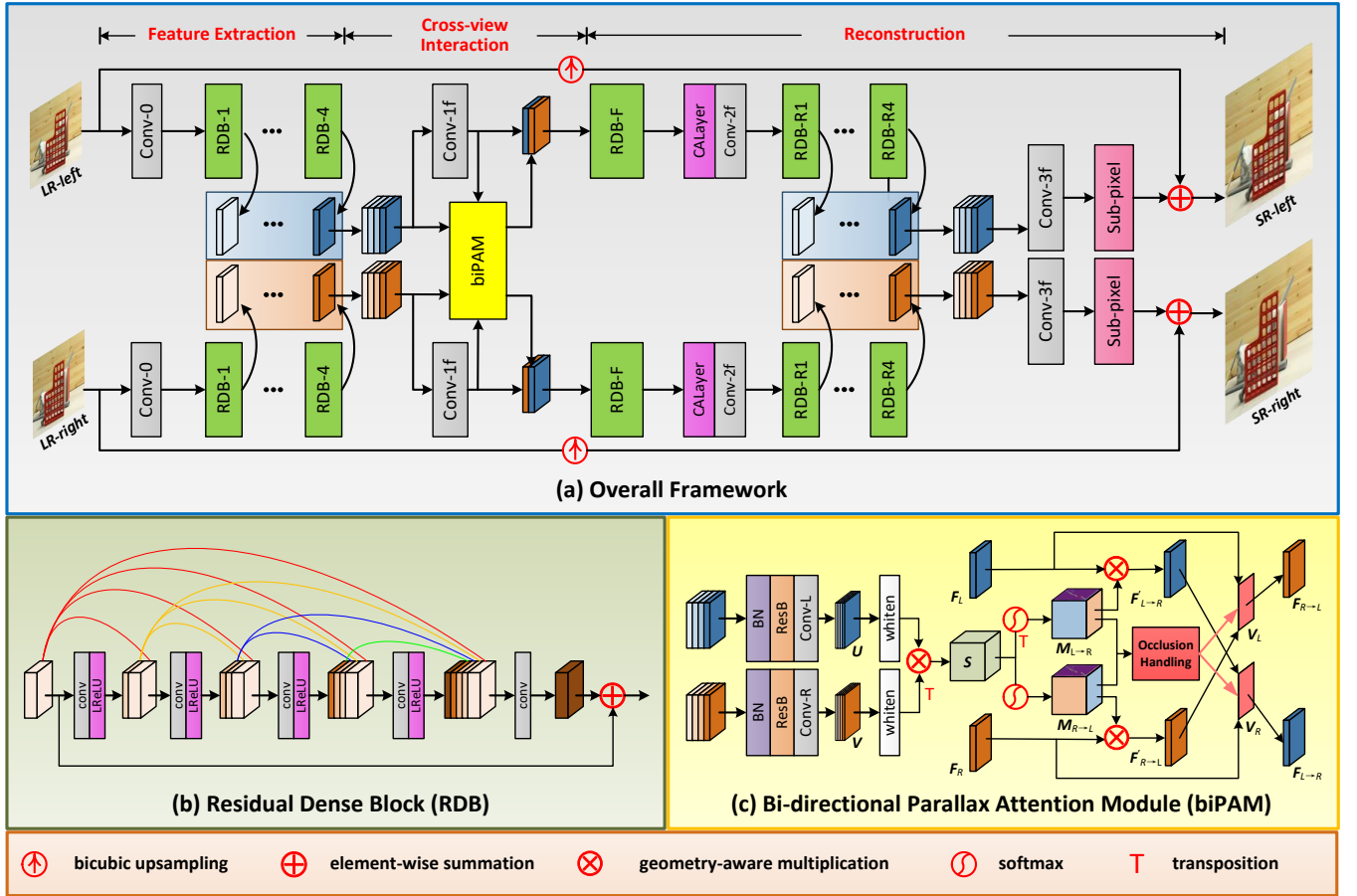


Fig. 2: An overview of our iPASSR network.

Specifically, they first explicitly estimated disparities using a pretrained stereo matching network [48] and then warped views to the other side to incorporate cross-view information.

III. METHOD

In this section, we introduce our method in details. Specifically, Section III-A introduces the architecture of our network. Section III-B describes our inline occlusion handling scheme. Section III-C describes our proposed losses.

A. Network Architecture

Our iPASSR network takes a pair of LR RGB stereo images \mathbf{I}_L^{input} and \mathbf{I}_R^{input} as its inputs to generate HR RGB stereo images \mathbf{I}_L^{SR} and \mathbf{I}_R^{SR} . As shown in Fig. 2(a), our network is highly symmetric and the weights of its left and right branches are shared. Given LR input stereo images, our network sequentially performs feature extraction, cross-view interaction, and reconstruction.

1) *Feature Extraction Module*: As shown in Fig. 2(b), we use the residual dense block (RDB) [13] as our basic block to generate features for both stereo correspondence estimation and image SR. The insights of using RDBs for feature extraction are two-fold: First, RDB can generate features with large receptive fields and dense sampling rates, which are beneficial to stereo correspondence estimation [49].

Second, RDB can fully use features from all the layers via local dense connection. The generated hierarchical features are demonstrated to be contributive to SR performance [13].

In our feature extraction module, input stereo images $\mathbf{I}_L^{input}, \mathbf{I}_R^{input} \in \mathbb{R}^{H \times W \times 3}$ are first fed to a convolution layer (i.e., *Conv-0*) to generate initial features $\mathbf{F}_L^0, \mathbf{F}_R^0 \in \mathbb{R}^{H \times W \times 64}$. These initial features are then fed to 4 cascaded RDBs for deep feature extraction. Within each RDB, we use 4 convolutions with a growth rate of 24 to achieve dense feature representation, and use 1 convolution for local feature fusion. That is, for the c^{th} ($c = 1, 2, 3, 4$) convolution in the k^{th} ($k = 1, 2, 3, 4$) RDB, the input feature is formed by concatenating the output features of the $(k-1)^{th}$ RDB with output features from all the preceding convolution layers in the k^{th} RDB, resulting in a channel number of $(64 + 24(c-1))$. For the last convolution layer used for local fusion, features from all preceding layers are concatenated to generate fused features with a channel number of 64 for local residual connection.

2) *Bi-directional Parallax Attention Module (biPAM)*: Since hierarchical feature representation is beneficial to stereo correspondence estimation, we form the inputs of our biPAM by concatenating the output features of each RDB in our feature extraction module. As shown in Fig. 2(c), the input stereo features are first fed to a batch-normalization (BN) layer and a transition residual block (i.e., *ResB*) to alleviate the

training conflict [2], [3], and then separately fed to 1×1 convolutions to generate $\mathbf{U}, \mathbf{V} \in \mathbb{R}^{H \times W \times 64}$. To achieve disentangled pairwise parallax attention, we follow [50] and feed \mathbf{U} and \mathbf{V} to a whitened layer to obtain normalized features \mathbf{U}' and \mathbf{V}' . That is,

$$\mathbf{U}'(h, w, c) = \mathbf{U}(h, w, c) - \frac{1}{W} \sum_{i=1}^W \mathbf{U}(h, i, c), \quad (1)$$

$$\mathbf{V}'(h, w, c) = \mathbf{V}(h, w, c) - \frac{1}{W} \sum_{i=1}^W \mathbf{V}(h, i, c). \quad (2)$$

To generate left and right attention maps, \mathbf{V}' is first transposed to $\mathbf{V}'^T \in \mathbb{R}^{H \times 64 \times W}$, and then performs a geometry-aware matrix multiplication (see Section III-B) with \mathbf{U}' to generate an initial score map $\mathbf{S} \in \mathbb{R}^{H \times W \times W}$. That is,

$$\mathbf{S} = \mathbf{U}' \otimes \mathbf{V}'^T, \quad (3)$$

where \otimes represents geometry-aware matrix multiplication, T represents transposition operation that exchanges the last two dimensions of a matrix. Afterwards, softmax normalization is applied to \mathbf{S} and \mathbf{S}^T along their third dimension to generate attention maps $\mathbf{M}_{R \rightarrow L} = \text{softmax}(\mathbf{S})$ and $\mathbf{M}_{L \rightarrow R} = \text{softmax}(\mathbf{S}^T)$, respectively.

To achieve cross-view interaction, both left and right features (generated by *Conv-1f* in Fig. 2(a)) need to be converted to the other side by taking a geometry-aware matrix multiplication with the corresponding attention maps. That is,

$$\mathbf{F}'_{R \rightarrow L} = \mathbf{M}_{R \rightarrow L} \otimes \mathbf{F}_R, \quad (4)$$

$$\mathbf{F}'_{L \rightarrow R} = \mathbf{M}_{L \rightarrow R} \otimes \mathbf{F}_L. \quad (5)$$

To avoid unreliable correspondence in occlusion regions, we propose an inline occlusion handling scheme in Section III-B to calculate valid masks \mathbf{V}_L and \mathbf{V}_R . The final converted features $\mathbf{F}_{R \rightarrow L}$ and $\mathbf{F}_{L \rightarrow R}$ can be obtained by

$$\mathbf{F}_{R \rightarrow L} = \mathbf{V}_L \odot \mathbf{F}'_{R \rightarrow L} + (\mathbf{1} - \mathbf{V}_L) \odot \mathbf{F}_L, \quad (6)$$

$$\mathbf{F}_{L \rightarrow R} = \mathbf{V}_R \odot \mathbf{F}'_{L \rightarrow R} + (\mathbf{1} - \mathbf{V}_R) \odot \mathbf{F}_R, \quad (7)$$

where \odot represents element-wise multiplication. Note that, values in \mathbf{V}_L and \mathbf{V}_R range from 0 (occluded) to 1 (non-occluded). According to Eqs. (6) and (7), occluded regions of converted features can be filled with the corresponding features from the target view, resulting in continuous spatial distributions.

3) *Reconstruction Module*: Similar to our feature extraction module, we use RDB as basic blocks in our reconstruction module. Taking the left branch as an example, the converted feature $\mathbf{F}_{R \rightarrow L}$ is first concatenated with \mathbf{F}_L and then fed to an RDB (i.e., *RDB-F*) for initial feature fusion. The output feature $\mathbf{F}_L^{\text{init}_f} \in \mathbb{R}^{H \times W \times 128}$ is then fed to a channel attention layer (i.e., *CALayer* [14]) and a convolution layer (i.e., *Conv-2f*) to produce the final fused feature $\mathbf{F}_L^f \in \mathbb{R}^{H \times W \times 64}$. Afterwards, \mathbf{F}_L^f is fed to 4 cascaded RDBs, a fusion layer (i.e., *Conv-3f*), and a sub-pixel layer [51] for final reconstruction.

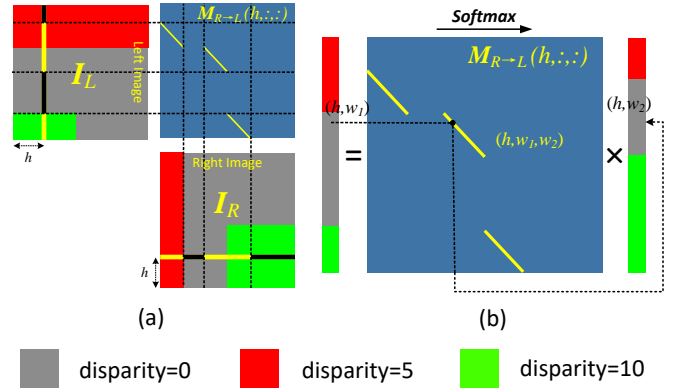


Fig. 3: A toy example to depict the stereo correspondence addressed by our biPAM. The gray, red, and green regions in \mathbf{I}_L and \mathbf{I}_R denote objects with a disparity of 0, 5, and 10 pixels, respectively. For simplicity, only a profile of $\mathbf{M}_{R \rightarrow L}$ at height h is visualized, which corresponds to the regions marked by yellow strokes in (a). Note that, occlusions (colored in black on the strokes) are implicitly encoded in the attention maps as empty intervals. (b) The right stroke can be converted into the left side by multiplying it with $\mathbf{M}_{R \rightarrow L}$.

B. Inline Occlusion Handling Scheme

Thanks to the aforementioned bi-directional parallax attention mechanism, the correspondence between left and right views can be generated in a symmetric manner. More importantly, the occlusions can be derived by checking the stereo consistency using the attention maps $\mathbf{M}_{R \rightarrow L}$ and $\mathbf{M}_{L \rightarrow R}$. In this subsection, we introduce our inline occlusion handling scheme in details.

Following [2], [3], we use a toy example to illustrate how occlusions are implicitly encoded in the parallax attention maps. Given a pair of stereo images \mathbf{I}_L and $\mathbf{I}_R \in \mathbb{R}^{H \times W}$, parallax attention maps $\mathbf{M}_{R \rightarrow L}, \mathbf{M}_{L \rightarrow R} \in \mathbb{R}^{H \times W \times W}$ can be generated following the operations in Section III-A2. As shown in Fig. 3(a), we visualize a profile of $\mathbf{M}_{R \rightarrow L}$ at height h (i.e., $\mathbf{M}_{R \rightarrow L}(h, :, :)$), which corresponds to the yellow strokes in the left and right images. In addition, black strokes represent occluded regions. It can be observed from Fig. 3(a) that: 1) occlusions occur near object edges where the depth values change suddenly, or occur near image boundaries (more specifically, left boundary of the left view and right boundary of the right view). 2) The occluded regions correspond to the empty intervals in the attention maps since their counterparts in the other view are unavailable. These two observations demonstrate that occlusions are implicitly encoded in the parallax attention maps. Consequently, occlusions can be obtained by checking the cycle consistency using $\mathbf{M}_{R \rightarrow L}$ and $\mathbf{M}_{L \rightarrow R}$. Specifically, the right image can be converted into the left side according to

$$\mathbf{I}_{R \rightarrow L} = \mathbf{M}_{R \rightarrow L} \otimes \mathbf{I}_R, \quad (8)$$

where \otimes represents the geometry-aware matrix multiplication. As shown in Fig. 3(b), the product of a slice of the right image (i.e., $\mathbf{I}_R(h, :)$) and the corresponding profile of the attention map (i.e., $\mathbf{M}_{R \rightarrow L}(h, :, :)$) determines the slice of the converted



Fig. 4: An illustration of valid masks generated by our occlusion handling scheme. For better visualization, we visualize $(1 - \mathbf{V}_L)$ and $(1 - \mathbf{V}_R)$. Red regions have large values and represent heavy occlusions.

left image at the same height (i.e., $\mathbf{I}_{R \rightarrow L}(h, :)$). All these resulting slices are concatenated to produce $\mathbf{I}_{R \rightarrow L}$.

Note that, softmax normalization has been performed along the third dimension of $\mathbf{M}_{R \rightarrow L}$ and $\mathbf{M}_{L \rightarrow R}$. Therefore, $\mathbf{M}_{R \rightarrow L}(h, w_1, w_2)$ can be considered as the matching possibility between $\mathbf{I}_R(h, w_2)$ and $\mathbf{I}_L(h, w_1)$. Furthermore, the possibility that $\mathbf{I}_L(h, w_1)$ is first converted to \mathbf{I}_R and then re-converted to $\mathbf{I}_L(h, w_1)$ can be calculated according to

$$\mathbf{P}_L(h, w_1) = \sum_{w_2=1}^W \mathbf{M}_{R \rightarrow L}(h, w_1, w_2) \cdot \mathbf{M}_{L \rightarrow R}(h, w_2, w_1). \quad (9)$$

Note that, $\mathbf{P}_L(h, w_1)$ is close to 0 if point (h, w_1) is occluded in the right view. Consequently, \mathbf{P}_L can be used to represent occlusions in the left image. Due to noise and rectification errors in stereo images, we relax the constraint in Eq. 9 by ± 2 pixels in this work:

$$\mathbf{P}'_L(h, w_1) = \sum_{\delta=-2}^2 \sum_{w_2=1}^W \mathbf{M}_{R \rightarrow L}(h, w_1 + \delta, w_2) \cdot \mathbf{M}_{L \rightarrow R}(h, w_2, w_1). \quad (10)$$

To maintain training stability, the left valid mask \mathbf{V}_L is calculated according to $\mathbf{V}_L = \tanh(5\mathbf{P}'_L)$. The right valid mask \mathbf{V}_R can be generated following a similar way. Visualization examples of the generated valid masks are shown in Fig. 4.

C. Losses

We introduce five losses to train our network. The overall loss function of our network is defined as:

$$\mathcal{L} = \mathcal{L}_{SR} + \lambda(\mathcal{L}_{photo} + \mathcal{L}_{cycle} + \mathcal{L}_{smooth} + \mathcal{L}_{cons}), \quad (11)$$

where \mathcal{L}_{SR} , \mathcal{L}_{photo} , \mathcal{L}_{cycle} , \mathcal{L}_{smooth} , and \mathcal{L}_{cons} represent SR loss, residual photometric loss, residual cycle loss, smoothness loss, and residual stereo consistency loss, respectively. λ represents the weight of the regularization term and was empirically set to 0.1 in this work.

The *SR loss* is defined as the L_1 distance between the super-resolved and groundtruth stereo images, i.e.,

$$\mathcal{L}_{SR} = \|\mathbf{I}_L^{SR} - \mathbf{I}_L^{HR}\|_1 + \|\mathbf{I}_R^{SR} - \mathbf{I}_R^{HR}\|_1, \quad (12)$$

where \mathbf{I}_L^{SR} and \mathbf{I}_R^{SR} represent the super-resolved left and right images, and \mathbf{I}_L^{HR} and \mathbf{I}_R^{HR} represent their groundtruth HR images, respectively.

Note that, all PAM-based stereo image SR methods [2]–[5] train their networks using photometric loss, cycle loss, and smoothness loss. That is, they learn stereo correspondence in an unsupervised manner and do not use groundtruth disparities during the training phase. However, illuminance variation in stereo vision can introduce problems to these methods. As shown in Fig. 5, due to exposure difference or non-Lambertian surfaces, the illuminance can vary significantly between left and right views. In this case, the photometric consistency and cycle consistency do not hold. Consequently, the photometric loss and cycle loss used in [2]–[5] can lead to mismatch and subsequently decrease the SR performance.

To handle this problem, we calculate these losses using residual images to improve their robustness to illuminance changes. Specifically, we introduce

$$\mathbf{X}_L = (|\mathbf{I}_L^{HR} - \mathbf{I}_L^{LR} \uparrow|) \downarrow, \quad (13)$$

$$\mathbf{X}_R = (|\mathbf{I}_R^{HR} - \mathbf{I}_R^{LR} \uparrow|) \downarrow, \quad (14)$$

where \uparrow and \downarrow represent bicubic upsampling and bicubic downsampling, respectively. \mathbf{X}_L and \mathbf{X}_R represent the absolute values of left and right residual images, respectively. Consequently, the residual photometric loss and residual cycle consistency loss can be calculated by

$$\mathcal{L}_{photo} = \|\mathbf{V}_L \odot (\mathbf{X}_L - \mathbf{M}_{R \rightarrow L} \otimes \mathbf{X}_R)\|_1 + \|\mathbf{V}_R \odot (\mathbf{X}_R - \mathbf{M}_{L \rightarrow R} \otimes \mathbf{X}_L)\|_1, \quad (15)$$

$$\mathcal{L}_{cycle} = \|\mathbf{V}_L \odot (\mathbf{X}_L - \mathbf{M}_{R \rightarrow L} \otimes \mathbf{M}_{L \rightarrow R} \otimes \mathbf{X}_L)\|_1 + \|\mathbf{V}_R \odot (\mathbf{X}_R - \mathbf{M}_{L \rightarrow R} \otimes \mathbf{M}_{R \rightarrow L} \otimes \mathbf{X}_R)\|_1. \quad (16)$$

The photometric and cycle losses calculated from residual images have two benefits. First, since illuminance components can be eliminated by computing residual images (see Fig. 5), more consistent and illuminance-robust stereo correspondence can be learned by our biPAM. Second, since residual images mainly contain high-frequency components, our biPAM can pay more attention to learn correspondence on texture-rich regions, which is contributive to SR performance (see Section IV-B3).

Apart from the aforementioned losses, we also use smoothness loss as in [2], [3] to regularize our biPAM. That is,

$$\mathcal{L}_{smooth} = \sum_{\mathbf{M}} \sum_{i,j,k} (\|\mathbf{M}(i, j, k) - \mathbf{M}(i+1, j, k)\|_1 + \|\mathbf{M}(i, j, k) - \mathbf{M}(i, j+1, k+1)\|_1), \quad (17)$$

where $\mathbf{M} \in \{\mathbf{M}_{R \rightarrow L}, \mathbf{M}_{L \rightarrow R}\}$. The first and second terms are used to achieve vertical and horizontal attention smoothness, respectively. For example, $\mathbf{M}_{R \rightarrow L}(i, j, k)$ represents the correspondence between $\mathbf{I}_R(i, k)$ and $\mathbf{I}_L(i, j)$. Therefore, the term $\|\mathbf{M}_{R \rightarrow L}(i, j, k) - \mathbf{M}_{R \rightarrow L}(i+1, j, k)\|_1$ enforces the correspondence between $\mathbf{I}_R(i+1, k)$ and $\mathbf{I}_L(i+1, j)$ to be close to the correspondence between $\mathbf{I}_R(i, k)$ and $\mathbf{I}_L(i, j)$. Consequently, smoothness in correspondence space can be encouraged.

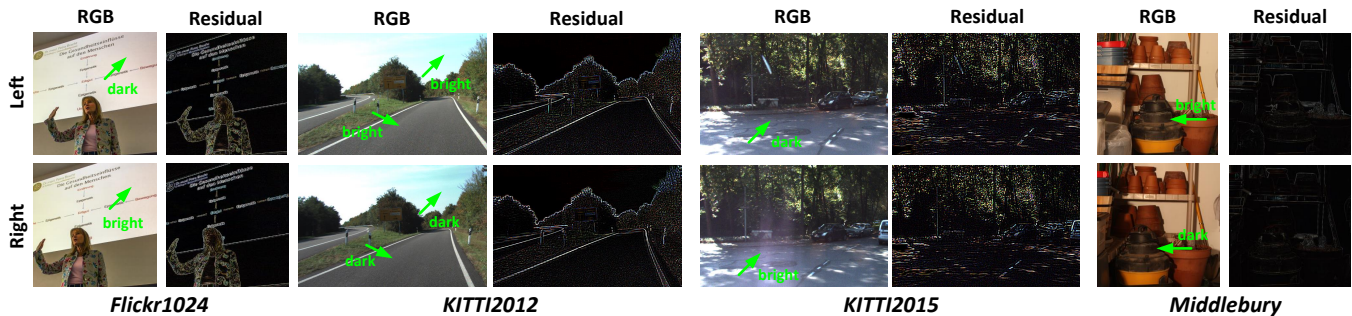


Fig. 5: An illustration of illuminance changes in stereo image pairs. Please view our [demo video](#) for better visualization.

Finally, we introduce our stereo consistency loss to ensure that a super-resolved view is close to the result converted from the other view. Similar to the aforementioned residual photometric loss, we also calculate our stereo consistency loss in LR residual space. The LR residuals between super-resolved images and groundtruth images are represented as

$$\mathbf{Y}_L = (|\mathbf{I}_L^{HR} - \mathbf{I}_L^{SR}|) \downarrow, \quad (18)$$

$$\mathbf{Y}_R = (|\mathbf{I}_R^{HR} - \mathbf{I}_R^{SR}|) \downarrow, \quad (19)$$

and the residual stereo consistency loss is defined as

$$\begin{aligned} \mathcal{L}_{cons} = & \|V_L \odot (\mathbf{Y}_L - \mathbf{M}_{R \rightarrow L} \otimes \mathbf{Y}_R)\|_1 \\ & + \|V_R \odot (\mathbf{Y}_R - \mathbf{M}_{L \rightarrow R} \otimes \mathbf{Y}_L)\|_1. \end{aligned} \quad (20)$$

IV. EXPERIMENTS

In this section, we first introduce the datasets and implementation details, then perform ablation studies to validate our design choices. Finally, we compare our iPASSR network to several state-of-the-art SISR and stereo image SR methods from different perspectives.

A. Datasets and Implementation Details

1) *Datasets*: During the training phase, we used 800 images from the training set of the Flickr1024 dataset [7] and 60 images from the Middlebury dataset [10] as training data. For images from the Middlebury dataset, we followed [1]–[4] to perform bicubic downsampling with a factor of 2 to generate HR images. During the test phase, we followed [1]–[4] to use 5 images from the Middlebury dataset [10], 20 images from the KITTI 2012 dataset [8] and 20 images from the KITTI 2015 dataset [9]. Furthermore, we used the test set provided by the Flickr1024 dataset [7] for additional evaluation.

2) *Implementation details*: We generated LR images by performing bicubic downsampling on HR images. During the training phase, the generated LR images were cropped into patches of size 30×90 with a stride of 20, and their HR counterparts were cropped accordingly. These patches were randomly flipped horizontally and vertically for data augmentation.

Peak signal-to-noise ratio (PSNR) and structural similarity (SSIM) index were used as quantitative metrics in this paper, and these metrics were calculated on RGB color space for

TABLE I: Quantitative results achieved on the KITTI 2015 dataset [9] by iPASSR with different cross-view information incorporation schemes for $4 \times SR$. Here, PSNR/SSIM values achieved on the left views are reported. Best results are in **bold faces**.

Models	Inputs	PSNR/SSIM
iPASSR with single input	Left	25.316/0.7753
iPASSR with replicated inputs	Left-Left	25.400/0.7775
Asymmetric iPASSR	Left-Right	25.548/0.7829
iPASSR	Left-Right	25.615/0.7850

performance evaluation. To achieve fair comparison with [1]–[4], we followed these methods to calculate PSNR and SSIM scores on the left views with their left boundaries (64 pixels) being cropped. Moreover, to comprehensively evaluate the performance of stereo image SR, we also report the average PSNR and SSIM scores on stereo image pairs (i.e., $(Left + Right) / 2$) without any boundary cropping.

Our network was implemented in PyTorch on a PC with two Nvidia RTX 2080Ti GPUs. All models were optimized using the Adam method with $\beta_1 = 0.9$, $\beta_2 = 0.999$ and a batch size of 36. The initial learning rate was set to 2×10^{-4} and reduced to half after every 30 epochs. The training was stopped after 80 epochs since more epochs do not provide further consistent improvement.

B. Ablation Study

In this subsection, we present ablation experiments to investigate our models and validate our design choices.

1) *Cross-view information*: To demonstrate the benefits introduced by cross-view information, we first removed biPAM and retrained a single branch of our iPASSR on the same training set as our original network. In addition, we also used pairs of replicated left images as inputs to directly perform inference using our original network. As shown in Table I, the network trained with single images (i.e., iPASSR with single input) suffers a decrease of 0.299 dB in PSNR (25.316 vs 25.615) and a decrease of 0.0097 in SSIM (0.7753 vs 0.7850) as compared to our original network. If replicated left images were used as inputs, the network (i.e., iPASSR with replicated inputs) achieves a PSNR score of 25.400 dB, which is also notably inferior to our original network. These results

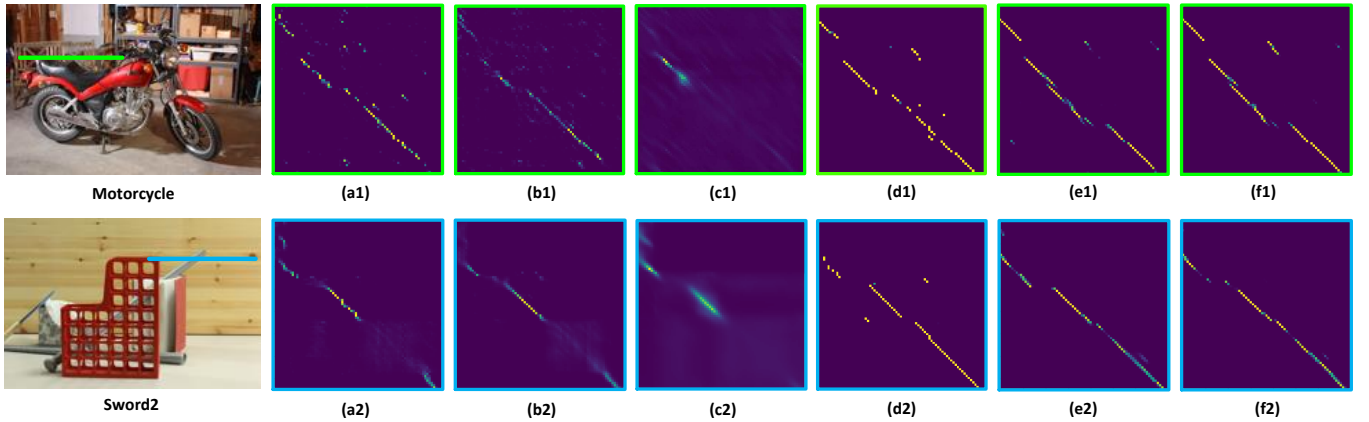


Fig. 6: Visualization of attention maps generated by iPASSR trained with different losses. (a) \mathcal{L}_{SR} , (b) $\mathcal{L}_{SR} + \lambda\mathcal{L}_{photo}$, (c) $\mathcal{L}_{SR} + \lambda(\mathcal{L}_{photo} + \mathcal{L}_{smooth})$, (d) $\mathcal{L}_{SR} + \lambda(\mathcal{L}_{photo} + \mathcal{L}_{cycle})$, (e) $\mathcal{L}_{SR} + \lambda(\mathcal{L}_{photo} + \mathcal{L}_{smooth} + \mathcal{L}_{cycle})$, (f) $\mathcal{L}_{SR} + \lambda(\mathcal{L}_{photo} + \mathcal{L}_{smooth} + \mathcal{L}_{cycle} + \mathcal{L}_{cons})$.

TABLE II: Quantitative results achieved on the KITTI 2015 dataset [9] by iPASSR with different losses for $4\times SR$. “Res” represents photometric loss, cycle loss, and stereo consistency loss calculated on residual images. Here, PSNR/SSIM values achieved on the left views are reported. Best results are in **bold faces**.

\mathcal{L}_{SR}	\mathcal{L}_{photo}	\mathcal{L}_{smooth}	\mathcal{L}_{cycle}	\mathcal{L}_{cons}	Res	PSNR/SSIM
✓						25.527/0.7827
✓	✓				✓	25.535/0.7815
✓	✓	✓			✓	25.481/0.7795
✓	✓		✓		✓	25.552/0.7839
✓	✓	✓	✓		✓	25.570/0.7839
✓	✓	✓	✓	✓		25.456/0.7775
✓	✓	✓	✓	✓	✓	25.615/0.7850

clearly demonstrate the significance of cross-view information for stereo image SR.

2) *Siamese network architecture*: We investigate the benefits introduced by our Siamese network architecture. Specifically, we retrained the network with stereo images as inputs, but only super-resolved the left view (which is similar to PASSRnet [2], [3]). It can be observed in Table I that this asymmetric network can achieve a PSNR score of 25.548 dB, which is marginally lower than our original network. This demonstrates that our Siamese network with symmetric structure can better exploit the cross-view information to improve the performance of stereo image SR.

3) *Losses*: We retrained our network using different losses to validate their effectiveness. As shown in Table II, the PSNR value of our network is decreased from 25.615 to 25.527 if only the SR loss is considered. That is because, without using the additional losses for regularization, our network cannot well incorporate cross-view information between stereo image pairs. In contrast, the SR performance is gradually improved if the photometric loss, cycle loss, smoothness loss, and stereo consistency loss are added. That is because, using these losses as regularization terms, our biPAM can focus on the most similar features to provide accurate correspondence. Moreover, an improvement of 0.159 dB (25.615 vs 25.456) in PSNR is introduced when the network is trained with these losses cal-

TABLE III: Comparative results achieved on the KITTI 2015 dataset by iPASSR with different settings in biPAM for $4\times SR$. Here, PSNR/SSIM values achieved on both the left images (i.e., *Left*) and on a pair of stereo images (i.e., $(Left + Right) / 2$) are reported. Best results are in **bold faces**.

Models	<i>Left</i>	$(Left + Right) / 2$
iPASSR w/o whiten layer	25.535/0.7830	26.125/0.8037
iPASSR w/o using valid mask	25.574/0.7843	26.179/0.8051
iPASSR	25.615/0.7850	26.316/0.8084

culated on residual images. As demonstrated in Section III-C, by applying these residual losses, the illuminance changes between stereo images can be eliminated and our biPAM can focus on high-frequency texture regions.

To better demonstrate the benefits introduced by different losses, we visualize the attention maps of scene *Motorcycle* and *Sword2* from the Middlebury dataset [10] in Fig. 6. It can be observed that the attention maps trained only with the SR loss suffer from heavy noise (e.g., Fig. 6 (a1)) and missing correspondence (Fig. 6 (a2)). When the photometric loss is introduced, the noise can be reduced but the problem of missing correspondence cannot be handled. That is because, the initial score map \mathbf{S} has similar values at different locations in textureless regions (e.g., regions marked by the blue stroke in scene *Sword2*). Consequently, a single point in the left view can be correlated to a number of points along the epipolar line in the right view, resulting in ambiguities in attention maps.

When the smoothness loss is added to the photometric loss, noise in the attention map can be eliminated but the problem of missing correspondence becomes more significant (see Figs. 6(c1) and (c2)), resulting in a 0.054 dB decrease (25.481 vs 25.535) in PSNR. In contrast, if the cycle loss is added to the photometric loss, the missing correspondence problem can be handled but the noise cannot be reduced, as shown in Figs. 6(d1). This problem can be handled by introducing both smoothness loss and cycle loss, as shown in Figs. 6 (e1) and (e2). Finally, the proposed stereo consistency loss can further enhance the stereo consistency to produce accurate and reasonable attention maps.

TABLE IV: Quantitative results achieved by different methods on the KITTI 2012 [8], KITTI 2015 [9], Middlebury [10], and Flickr1024 [7] datasets. #P represents the number of parameters of the networks. Here, PSNR/SSIM values achieved on both the left images (i.e., *Left*) and a pair of stereo images (i.e., $(Left + Right) / 2$) are reported. The best results are in **bold faces** and the second best results are underlined.

Method	Scale	#P	<i>Left</i>			$(Left + Right) / 2$			
			KITTI 2012	KITTI 2015	Middlebury	KITTI 2012	KITTI 2015	Middlebury	Flickr1024
Bicubic	2×	—	28.44/0.8808	27.81/0.8814	30.46/0.8979	28.51/0.8842	28.61/0.8973	30.60/0.8990	24.94/0.8186
VDSR	2×	0.66M	30.17/0.9062	28.99/0.9038	32.66/0.9101	30.30/0.9089	29.78/0.9150	32.77/0.9102	25.60/0.8534
EDSR	2×	38.6M	30.83/0.9199	29.94/ <u>0.9231</u>	<u>34.84/0.9489</u>	<u>30.96/0.9228</u>	30.73/0.9335	34.95/0.9492	28.66/0.9087
RDN	2×	22.0M	30.81/0.9197	29.91/0.9224	34.85/0.9488	30.94/0.9227	30.70/0.9330	34.94/0.9491	<u>28.64/0.9084</u>
RCAN	2×	15.3M	<u>30.88/0.9202</u>	<u>29.97/0.9231</u>	34.80/0.9482	31.02/0.9232	<u>30.77/0.9336</u>	34.90/0.9486	28.63/0.9082
StereoSR	2×	1.08M	29.42/0.9040	28.53/0.9038	33.15/0.9343	29.51/0.9073	29.33/0.9168	33.23/0.9348	25.96/0.8599
PASSRnet	2×	1.37M	30.68/0.9159	29.81/0.9191	34.13/0.9421	30.81/0.9190	30.60/0.9300	34.23/0.9422	28.38/0.9038
iPASSR (ours)	2×	1.37M	30.97/0.9210	30.01/0.9234	34.41/0.9454	31.11/0.9240	30.81/0.9340	34.51/0.9454	28.60/ 0.9097
Bicubic	4×	—	24.52/0.7310	23.79/0.7072	26.27/0.7553	24.58/0.7372	24.38/0.7340	26.40/0.7572	21.82/0.6293
VDSR	4×	0.66M	25.54/0.7662	24.68/0.7456	27.60/0.7933	25.60/0.7722	25.32/0.7703	27.69/0.7941	22.46/0.6718
EDSR	4×	38.9M	26.26/0.7954	25.38/0.7811	<u>29.15/0.8383</u>	26.35/0.8015	26.04/0.8039	29.23/ <u>0.8397</u>	23.46/0.7285
RDN	4×	22.0M	26.23/0.7952	25.37/0.7813	<u>29.15/0.8387</u>	26.32/0.8014	26.04/0.8043	<u>29.27/0.8404</u>	<u>23.47/0.7295</u>
RCAN	4×	15.4M	<u>26.36/0.7968</u>	<u>25.53/0.7836</u>	29.20/0.8381	<u>26.44/0.8029</u>	<u>26.22/0.8068</u>	29.30/0.8397	23.48/0.7286
PASSRnet	4×	1.42M	26.26/0.7919	25.41/0.7772	28.61/0.8232	26.34/0.7981	26.08/0.8002	28.72/0.8236	23.31/0.7195
SRRes+SAM	4×	1.73M	26.35/0.7957	<u>25.55/0.7825</u>	28.76/0.8287	<u>26.44/0.8018</u>	26.22/0.8054	28.83/0.8290	23.27/0.7233
iPASSR (ours)	4×	1.42M	26.47/0.7993	25.61/0.7850	29.07/0.8363	26.56/0.8053	26.32/0.8084	29.16/0.8367	23.44/ <u>0.7287</u>

Note: We do not present 2×SR results of SRRes+SAM [4] and 4×SR results of StereoSR [1] since their models are unavailable.

4) *Whiten layer*: We validate the effectiveness of whiten layers by removing them from our biPAM. As shown in Table III, the average PSNR value suffers a decrease of 0.191 dB (i.e., 26.316 vs 26.125) if whiten layers are removed. Since the average values of queries and keys are subtracted by the whiten operation (i.e., Eqs. (1) and (2)), more robust pairwise correspondence can be generated in non-local attention mechanisms [50]. Experimental results in Table III further demonstrate the effectiveness of whiten operations in our parallax attention mechanism.

5) *Valid mask*: We demonstrate the effectiveness of valid mask by removing it from both our network and our losses. That is, the converted features in biPAM are directly concatenated with the original features on the target side without using Eqs. (6) and (7). Meanwhile, the photometric loss, cycle loss, and stereo consistency loss are applied equally to all spatial locations without considering occlusions. It can be observed in Table III that the average PSNR value¹ suffers a decrease of 0.137 dB (i.e., 26.316 to 26.179) if the valid mask is not used. This demonstrates the effectiveness of our valid masks.

C. Comparison to the State-of-the-arts

In this section, we compare our iPASSR to several state-of-the-art methods, including four SISR methods² (i.e., VDSR [20], EDSR [12], RDN [13], RCAN [14]) and three stereo

image SR methods³ (i.e., StereoSR [1], PASSRnet [2], [3], SRResNet+SAM [4]). We also include bicubic interpolation as a baseline method. Moreover, to achieve fair comparison with SISR methods, we retrained these methods [12]–[14], [20] on the same training datasets as our method. We also analyze the influence of difference training set on EDSR and RCAN in Section IV-D.

1) *Quantitative Results*: Quantitative results are shown in Table IV. To achieve fair comparison with StereoSR [1] and PASSRnet [2], [3], we present the results achieved on the left images with their left boundary (64 pixels) being cropped. We also report the average PSNR and SSIM values on both sides of views for comprehensive evaluation. Note that, the super-resolved right images of StereoSR [1] and PASSRnet [2], [3] can be obtained by exchanging the left/right input images of their networks.

It can be observed in Table IV that our iPASSR achieves the highest PSNR and SSIM values on the KITTI 2012 [8] and KITTI 2015 [9] datasets for both 2× and 4×SR. For the Middlebury [10] and Flickr1024 [7] datasets, our iPASSR outperforms all stereo image SR methods [1]–[4], but is inferior to EDSR [12], RDN [13], and RCAN [14]. Note that, the model sizes of our iPASSR are comparable to PASSRnet (i.e., 1.37M for 2×SR and 1.42M for 4×SR), which are smaller than these SISR methods [12]–[14] by more than one order of magnitude. As demonstrated in [12]–[14], a deep and large SR model enables rich and hierarchical feature representation (i.e., enhance intra-view information exploitation) and thus can significantly boost the SR performance. Differently, our

¹Here, we use the average PSNR/SSIM values of a stereo image pair for comparison since occlusions generally occur at image boundaries, but the leftmost 64 pixels were excluded when performing evaluation on the left views (see Sec IV-A2).

²Note that, DRCN [52], DRRN [53], and LapSRN [54] were not included for comparison in this paper since they have been outperformed by PASSRnet as demonstrated in [2], [3].

³We do not compare our method to SPAMnet [5] and DASSR [6] because: 1) their codes and models are unavailable, 2) The evaluation schemes in [5], [6] are different from those in [1]–[4], so that we cannot directly copy the PSNR and SSIM values in their papers.

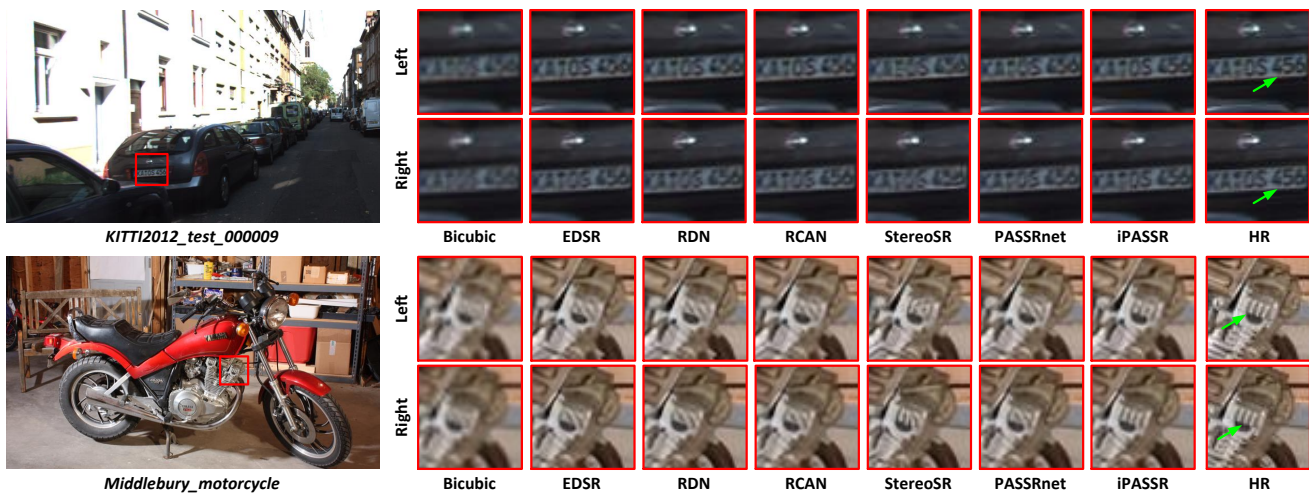


Fig. 7: Visual results achieved by different methods on the KITTI 2012 [8] and Middlebury [10] datasets for $2\times$ SR.



Fig. 8: Visual results achieved by different methods on the KITTI 2015 [9] and Flickr1024 [7] datasets for $4\times$ SR.

iPASSR improves SR performance by using a lightweight model to exploit cross-view information in stereo images, and thus significantly reduces the performance gap between heavy models (e.g., 28.60 to 28.66 for $2\times$ SR and 23.44 to 23.48 for $4\times$ SR on the Flickr1024 dataset [7]).

2) *Qualitative Results*: Qualitative results for $2\times$ and $4\times$ SR are shown in Figs. 7 and 8, respectively. A [demo video](#) is also provided for better visual comparison. It can be observed from zoom-in regions that our iPASSR can well recover textures and details with fewer artifacts. In contrast, state-of-the-art SISR methods [12]–[14] produce over-smoothed images with poor details (e.g., the horizontal stripes in scene *Flickr1024_test_0089* in Fig. 8), or generate images with more artifacts (e.g., wheels in scene *KITTI2015_test_000007* in Fig. 8). Since input LR images are degraded by the downsampling operation, the SR process is highly ill-posed, especially for $4\times$ SR. In such cases, SISR methods which only use spatial information for SR cannot reliably recover missing details. In contrast, our iPASSR can use complementary cross-

view information provided by stereo images to produce more faithful details. It is also worth noting that, since we enhance stereo consistency by exploiting symmetries at module level, network level and optimization level, our iPASSR can produce more stereo-consistent results (i.e., perform well on both left and right views) than PASSRnet [2], [3] and SRResNet+SAM [4]. These qualitative results clearly demonstrate the effectiveness of our iPASSR.

3) *Performance on Real-World Images*: We compare the performance of different methods on real-world stereo images by directly applying them to the original images in the Flickr1024 [7] dataset. As shown in Fig. 9, our method produces images with more faithful details and less artifacts, which demonstrates the promising generalization ability of our iPASSR to real-world images. It is worth noting that, left and right views of an image pair may suffer different degrees of degradation in real-world cases. For example, in the red boxes of scene *Flickr1024_test_0023*, the left image suffers more severe blurs than the right image. Based on the intra-view

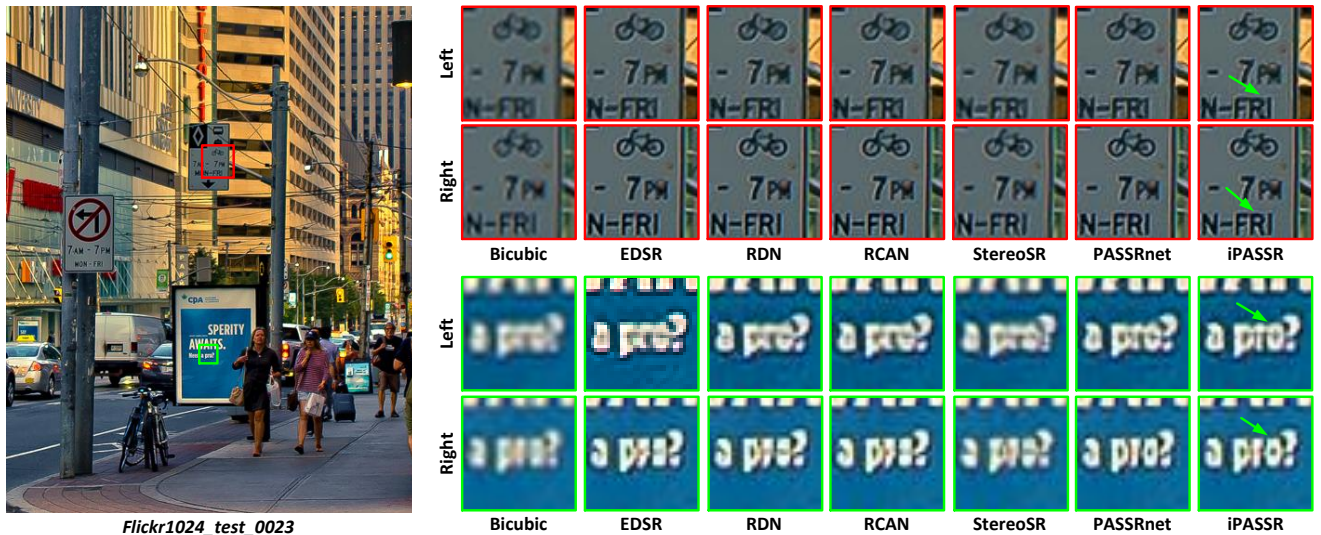


Fig. 9: Visual results achieved by different methods on real-world images [7] for $2\times$ SR.

TABLE V: Quantitative results achieved by GwcNet [55] using $4\times$ SR stereo images generated by different SR methods. All these metrics were averaged on the test set of the SceneFlow dataset [56], where lower values indicate better performance. Best results are in **bold faces** and the second best results are underlined.

Method	EPE	$>1px$ (%)	$>2px$ (%)	$>3px$ (%)
Bicubic	1.196	11.5	5.96	4.28
VDSR [20]	1.068	10.8	5.37	3.80
PASSRnet [2], [3]	1.019	11.5	5.44	3.72
SRRes+SAM [4]	0.991	11.1	5.18	3.57
iPASSR (ours)	<u>0.949</u>	<u>10.0</u>	<u>4.79</u>	<u>3.35</u>
HR	0.667	6.77	3.34	2.38

information only, state-of-the-art SISR methods cannot well recover the details in the left view. In contrast, our method benefits a lot from the right view with less blurring artifacts.

4) *Benefits to Disparity Estimation*: Since high-resolution and stereo-consistent image pairs are beneficial to disparity estimation, we investigate the benefits introduced by different SR methods by using their super-resolved stereo images to perform disparity estimation. Specifically, we first downsampled the images on the test sets⁴ of the SceneFlow dataset [56] by 4 times to generate LR images, and then used different SR methods to super-resolve these LR images to their original resolution. Afterwards, we applied GwcNet [55] to these super-resolved stereo images to perform disparity estimation. Note that, the original HR images and images generated by bicubic upsampling method were used to produce upper bound and baseline results, respectively. We used end-point-error (EPE) and t-pixel error rate ($> tpx$) as quantitative metrics to evaluate the estimated disparity. As shown in Table V, input stereo images have a significant influence on the performance of disparity estimation. Specifically, a 0.529 (i.e., 79.3%)

⁴All 145 scenes under path “./TEST/C/” were used as the test set in this paper. For stereo images of each scene, only the first frame (i.e., “./left/0006.png” and “./right/0006.png”) was used.

TABLE VI: Comparative results achieved by EDSR [12] and RCAN [14] with different training set for both $2\times$ and $4\times$ SR.

Method	KITTI 2012	KITTI 2015	Middlebury	Flickr1024
EDSR_div2k ($2\times$)	31.06/0.925	30.77/0.935	35.34/0.951	28.58/0.909
EDSR_stereo ($2\times$)	30.95/0.923	30.73/0.934	34.95/0.949	28.66/0.908
RCAN_div2k ($2\times$)	31.16/0.926	30.88/0.945	35.42/0.952	28.64/0.910
RCAN_stereo ($2\times$)	31.02/0.923	30.77/0.934	34.90/0.949	28.63/0.908
EDSR_div2k ($4\times$)	26.62/0.809	26.39/0.814	29.48/0.842	23.58/0.735
EDSR_stereo ($4\times$)	26.35/0.802	26.04/0.804	29.23/0.840	23.46/0.729
RCAN_div2k ($4\times$)	26.65/0.809	26.45/0.814	29.56/0.845	23.60/0.737
RCAN_stereo ($4\times$)	26.44/0.803	26.22/0.807	29.30/0.840	23.48/0.729

increase in EPE is introduced when HR input stereo images are replaced with the bicubically interpolated ones. It demonstrates that the details (e.g., edges and textures) in the stereo images are very significant to disparity estimation. Note that, the accuracy of disparity estimation can be improved if input LR stereo images are first super-resolved by SR methods. As compared to SISR [20] and stereo image SR [2]–[4] methods, our method can improve the accuracy of disparity estimation (i.e., reduce the EPE and t-pixel error rate) to the largest extent by providing high-quality and stereo-consistent input stereo images. Figure 10 illustrates some qualitative results achieved on several scenes. It can be observed that the disparity maps estimated from images generated by our method are more accurate and close to the ones estimated from the original HR stereo images.

D. Discussion

During the retraining of these SISR methods [12]–[14], we noticed that the training dataset has a significant influence on their SR performance. As shown in Table VI, EDSR and RCAN achieve better SR performance when trained on the DIV2K dataset [57]. The performance improvements are very significant on the Middlebury dataset for $2\times$ SR and on all the datasets for $4\times$ SR. That is because, the DIV2K dataset was specifically developed for SISR and has higher quality images than existing stereo image datasets. To further

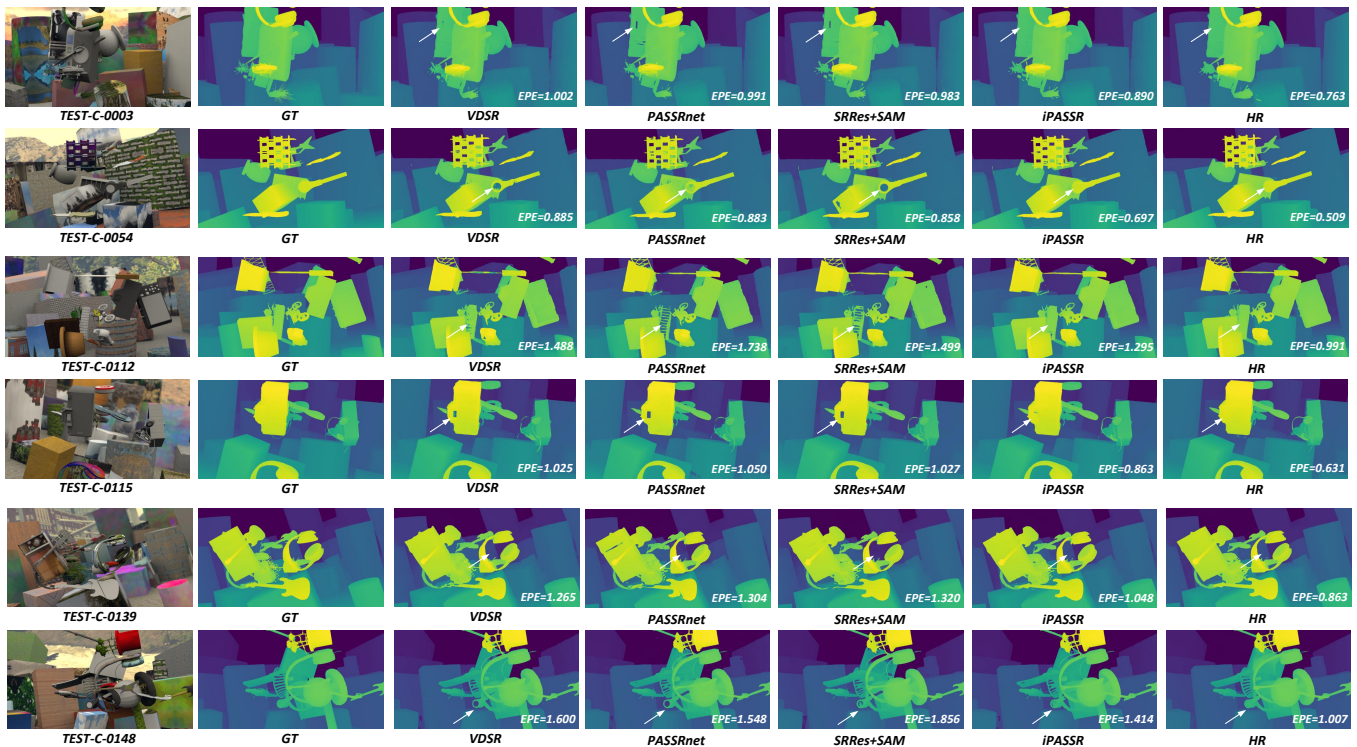


Fig. 10: Disparity estimation results achieved by GwcNet [55] using $4\times$ SR stereo images generated by different SR methods.

TABLE VII: No-reference perceptual quality metrics of different SR datasets. Both the average value and the standard deviation are reported. Lower scores of BRISQUE [58], NIQE [59] and higher scores of CEIQ [60] indicate better quality. Best results are in **bold faces**.

Dataset	BRISQUE (\downarrow)	NIQE (\downarrow)	CEIQ (\uparrow)
KITTI 2012	17.30 (± 6.60)	3.22 (± 0.42)	3.31 (± 0.14)
KITTI 2015	26.41 (± 5.26)	3.23 (± 0.48)	3.34 (± 0.19)
Middlebury	14.88 (± 9.19)	3.77 (± 0.99)	3.31 (± 0.21)
Flickr1024	19.10 (± 13.57)	3.40 (± 0.99)	3.25 (± 0.36)
DIV2K	11.40 (± 11.98)	2.99 (± 1.05)	3.36 (± 0.30)

demonstrate the quality gap between existing stereo image datasets [7]–[10] and the DIV2K dataset, we use three no-reference image quality assessment (NRIQA) metrics (i.e., BRISQUE [58], NIQE [59], and CEIQ [60]) to evaluate the image quality of these datasets. As shown in Table VII, the DIV2K dataset achieves the best results in all the three metrics, which demonstrates that the images in this dataset are of higher quality than those in the stereo image datasets. The experimental results in Tables VI and VII clearly demonstrate that high-quality training samples can introduce a notable performance gain to deep SR networks.

V. CONCLUSION AND FUTURE WORK

In this paper, we proposed to exploit symmetry cues for stereo image SR. Specifically, we first designed a bi-directional parallax attention module (biPAM) and an inline occlusion handling scheme to effectively interact cross-view information. Then, we equipped biPAM to our Siamese network to

achieve high-quality stereo image SR. For optimization, we proposed several losses to achieve robustness to illuminance changes. Experimental results on the KITTI 2012, KITTI 2015, Middlebury, and Flickr1024 datasets have demonstrated the superiority of our method. Compared to our previous PASSRnet, the proposed iPASSR can achieve a notable performance improvement with comparable model sizes.

As discussed in Section IV-D, the high-quality training samples can introduce significant performance improvements to SR methods by enhancing their intra-view information exploitation capability. However, the high-quality single image datasets such as DIV2K [57] cannot be directly used to train stereo image SR methods. Therefore, it is still an open issue to make stereo image SR methods more powerful in intra-view information exploitation. To handle this problem, a straightforward strategy is to develop a high-quality dataset specifically designed for stereo image SR. However, developing large-scale datasets with diverse scenarios under stereo settings is relatively labor-intensive. Another solution is to design novel algorithms (e.g., knowledge transfer [61]) that can effectively learn natural context priors from SISR dataset for stereo image SR. In the future, we will investigate the aforementioned schemes to further improve the performance of stereo image SR methods.

REFERENCES

- [1] D. S. Jeon, S.-H. Baek, I. Choi, and M. H. Kim, “Enhancing the spatial resolution of stereo images using a parallax prior,” in *Proceedings of the IEEE Conference on Computer Vision and Pattern Recognition (CVPR)*, 2018, pp. 1721–1730. 1, 2, 6, 8

- [2] L. Wang, Y. Wang, Z. Liang, Z. Lin, J. Yang, W. An, and Y. Guo, "Learning parallax attention for stereo image super-resolution," in *IEEE Conference on Computer Vision and Pattern Recognition (CVPR)*, 2019. 1, 2, 4, 5, 6, 7, 8, 9, 10
- [3] L. Wang, Y. Guo, Y. Wang, Z. Liang, Z. Lin, J. Yang, and W. An, "Parallax attention for unsupervised stereo correspondence learning," *IEEE Transactions on Pattern Analysis and Machine Intelligence*, 2020. 1, 2, 4, 5, 6, 7, 8, 9, 10
- [4] X. Ying, Y. Wang, L. Wang, W. Sheng, W. An, and Y. Guo, "A stereo attention module for stereo image super-resolution," *IEEE Signal Processing Letters*, vol. 27, pp. 496–500, 2020. 1, 2, 5, 6, 8, 9, 10
- [5] W. Song, S. Choi, S. Jeong, and K. Sohn, "Stereoscopic image super-resolution with stereo consistent feature," in *AAAI Conference on Artificial Intelligence*, 2020, pp. 12 031–12 038. 1, 2, 5, 8
- [6] B. Yan, C. Ma, B. Bare, W. Tan, and S. C. H. Hoi, "Disparity-aware domain adaptation in stereo image restoration," in *IEEE Conference on Computer Vision and Pattern Recognition (CVPR)*, 2020. 1, 2, 8
- [7] Y. Wang, L. Wang, J. Yang, W. An, and Y. Guo, "Flickr1024: A large-scale dataset for stereo image super-resolution," in *The IEEE International Conference on Computer Vision (ICCV) Workshops*, Oct 2019, pp. 3852–3857. 1, 2, 6, 8, 9, 10, 11
- [8] A. Geiger, P. Lenz, and R. Urtasun, "Are we ready for autonomous driving? the kitti vision benchmark suite," in *Proceedings of the IEEE Conference on Computer Vision and Pattern Recognition (CVPR)*, 2012. 2, 6, 8, 9, 11
- [9] M. Menze and A. Geiger, "Object scene flow for autonomous vehicles," in *Proceedings of the IEEE Conference on Computer Vision and Pattern Recognition (CVPR)*, 2015, pp. 3061–3070. 2, 6, 7, 8, 9, 11
- [10] D. Scharstein, H. Hirschmüller, Y. Kitajima, G. Krathwohl, N. Nešić, X. Wang, and P. Westling, "High-resolution stereo datasets with subpixel-accurate ground truth," in *German Conference on Pattern Recognition*. Springer, 2014, pp. 31–42. 2, 6, 7, 8, 9, 11
- [11] J. Li, F. Fang, K. Mei, and G. Zhang, "Multi-scale residual network for image super-resolution," in *European Conference on Computer Vision (ECCV)*, 2018, pp. 517–532. 2
- [12] B. Lim, S. Son, H. Kim, S. Nah, and K. Mu Lee, "Enhanced deep residual networks for single image super-resolution," in *IEEE Conference on Computer Vision and Pattern Recognition Workshops (CVPRW)*, 2017, pp. 136–144. 2, 8, 9, 10
- [13] Y. Zhang, Y. Tian, Y. Kong, B. Zhong, and Y. Fu, "Residual dense network for image super-resolution," in *IEEE Conference on Computer Vision and Pattern Recognition (CVPR)*, 2018, pp. 2472–2481. 2, 3, 8, 9, 10
- [14] Y. Zhang, K. Li, K. Li, L. Wang, B. Zhong, and Y. Fu, "Image super-resolution using very deep residual channel attention networks," in *European Conference on Computer Vision (ECCV)*, 2018, pp. 286–301. 2, 4, 8, 9, 10
- [15] T. Dai, J. Cai, Y. Zhang, S.-T. Xia, and L. Zhang, "Second-order attention network for single image super-resolution," in *IEEE Conference on Computer Vision and Pattern Recognition (CVPR)*, 2019, pp. 11 065–11 074. 2
- [16] C. Ledig, L. Theis, F. Huszár, J. Caballero, A. Cunningham, A. Acosta, A. Aitken, A. Tejani, J. Totz, Z. Wang *et al.*, "Photo-realistic single image super-resolution using a generative adversarial network," in *IEEE Conference on Computer Vision and Pattern Recognition (CVPR)*, 2017, pp. 4681–4690. 2
- [17] X. Wang, K. Yu, S. Wu, J. Gu, Y. Liu, C. Dong, Y. Qiao, and C. Change Loy, "Esrgan: Enhanced super-resolution generative adversarial networks," in *European Conference on Computer Vision (ECCV)*, 2018, pp. 0–0. 2
- [18] W. Zhang, Y. Liu, C. Dong, and Y. Qiao, "Ranksrgan: Generative adversarial networks with ranker for image super-resolution," in *Proceedings of the IEEE International Conference on Computer Vision (ICCV)*, 2019, pp. 3096–3105. 2
- [19] C. Dong, C. C. Loy, K. He, and X. Tang, "Learning a deep convolutional network for image super-resolution," in *European Conference on Computer Vision (ECCV)*. Springer, 2014, pp. 184–199. 2
- [20] J. Kim, J. Kwon Lee, and K. Mu Lee, "Accurate image super-resolution using very deep convolutional networks," in *IEEE Conference on Computer Vision and Pattern Recognition (CVPR)*, 2016, pp. 1646–1654. 2, 8, 10
- [21] K. He, X. Zhang, S. Ren, and J. Sun, "Deep residual learning for image recognition," in *IEEE Conference on Computer Vision and Pattern Recognition (CVPR)*, 2016, pp. 770–778. 2
- [22] G. Huang, Z. Liu, L. Van Der Maaten, and K. Q. Weinberger, "Densely connected convolutional networks," in *IEEE Conference on Computer Vision and Pattern Recognition (CVPR)*, 2017, pp. 4700–4708. 2
- [23] R. Liao, X. Tao, R. Li, Z. Ma, and J. Jia, "Video super-resolution via deep draft-ensemble learning," in *Proceedings of the IEEE International Conference on Computer Vision (ICCV)*, 2015, pp. 531–539. 2
- [24] L. Wang, Y. Guo, Z. Lin, X. Deng, and W. An, "Learning for video super-resolution through hr optical flow estimation," in *Asian Conference on Computer Vision (ACCV)*. Springer, 2018, pp. 514–529. 2
- [25] L. Wang, Y. Guo, L. Liu, Z. Lin, X. Deng, and W. An, "Deep video super-resolution using HR optical flow estimation," *IEEE Transactions on Image Processing*, vol. 29, pp. 4323–4336, 2020. 2
- [26] X. Tao, H. Gao, R. Liao, J. Wang, and J. Jia, "Detail-revealing deep video super-resolution," in *Proceedings of the IEEE International Conference on Computer Vision (ICCV)*, 2017, pp. 4472–4480. 2
- [27] S. Li, F. He, B. Du, L. Zhang, Y. Xu, and D. Tao, "Fast spatio-temporal residual network for video super-resolution," in *Proceedings of the IEEE Conference on Computer Vision and Pattern Recognition (CVPR)*, 2019, pp. 10 522–10 531. 2
- [28] X. Ying, L. Wang, Y. Wang, W. Sheng, W. An, and Y. Guo, "Deformable 3d convolution for video super-resolution," *IEEE Signal Processing Letters*, 2020. 2
- [29] Y. Jo, S. Wug Oh, J. Kang, and S. Joo Kim, "Deep video super-resolution network using dynamic upsampling filters without explicit motion compensation," in *Proceedings of the IEEE Conference on Computer Vision and Pattern Recognition (CVPR)*, 2018, pp. 3224–3232. 2
- [30] Y. Tian, Y. Zhang, Y. Fu, and C. Xu, "Tdan: Temporally deformable alignment network for video super-resolution," *IEEE Conference on Computer Vision and Pattern Recognition (CVPR)*, 2020. 2
- [31] X. Wang, K. C. Chan, K. Yu, C. Dong, and C. Change Loy, "Edvr: Video restoration with enhanced deformable convolutional networks," in *IEEE Conference on Computer Vision and Pattern Recognition Workshops (CVPRW)*, 2019. 2
- [32] X. Xiang, Y. Tian, Y. Zhang, Y. Fu, A. Jan, and C. Xu, "Zooming slowmo: Fast and accurate one-stage space-time videosuper-resolution," in *IEEE Conference on Computer Vision and Pattern Recognition (CVPR)*, 2020. 2
- [33] Y. Yoon, H.-G. Jeon, D. Yoo, J.-Y. Lee, and I. So Kweon, "Learning a deep convolutional network for light-field image super-resolution," in *IEEE International Conference on Computer Vision Workshops (ICCVW)*, 2015, pp. 24–32. 2
- [34] Y. Yoon, H.-G. Jeon, D. Yoo, J.-Y. Lee, and I. S. Kweon, "Light-field image super-resolution using convolutional neural network," *IEEE Signal Processing Letters*, vol. 24, no. 6, pp. 848–852, 2017. 2
- [35] Y. Wang, F. Liu, K. Zhang, G. Hou, Z. Sun, and T. Tan, "Lfnet: A novel bidirectional recurrent convolutional neural network for light-field image super-resolution," *IEEE Transactions on Image Processing*, vol. 27, no. 9, pp. 4274–4286, 2018. 2
- [36] S. Zhang, Y. Lin, and H. Sheng, "Residual networks for light field image super-resolution," in *IEEE Conference on Computer Vision and Pattern Recognition (CVPR)*, 2019, pp. 11 046–11 055. 2
- [37] N. Meng, H. K.-H. So, X. Sun, and E. Lam, "High-dimensional dense residual convolutional neural network for light field reconstruction," *IEEE Transactions on Pattern Analysis and Machine Intelligence*, 2019. 2
- [38] N. Meng, X. Wu, J. Liu, and E. Y. Lam, "High-order residual network for light field super-resolution," *AAAI Conference on Artificial Intelligence*, 2020. 2
- [39] Y. Wang, J. Yang, L. Wang, X. Ying, T. Wu, W. An, and Y. Guo, "Light field image super-resolution using deformable convolution," *arXiv preprint arXiv:2007.03535*, 2020. 2
- [40] Y. Wang, L. Wang, J. Yang, W. An, J. Yu, and Y. Guo, "Spatial-angular interaction for light field image super-resolution," in *European Conference on Computer Vision (ECCV)*, 2020. 2
- [41] H. Zheng, M. Ji, H. Wang, Y. Liu, and L. Fang, "Crossnet: An end-to-end reference-based super resolution network using cross-scale warping," in *European Conference on Computer Vision (ECCV)*, 2018, pp. 88–104. 2
- [42] Z. Zhang, Z. Wang, Z. Lin, and H. Qi, "Image super-resolution by neural texture transfer," in *IEEE Conference on Computer Vision and Pattern Recognition (CVPR)*, 2019, pp. 7982–7991. 2
- [43] F. Yang, H. Yang, J. Fu, H. Lu, and B. Guo, "Learning texture transformer network for image super-resolution," in *IEEE Conference on Computer Vision and Pattern Recognition (CVPR)*, 2020, pp. 5791–5800. 2
- [44] Y. Xie, J. Xiao, M. Sun, C. Yao, and K. Huang, "Feature representation matters: End-to-end learning for reference-based image super-resolution," in *European Conference on Computer Vision (ECCV)*, 2020. 2

- [45] H. Yue, X. Sun, J. Yang, and F. Wu, "Landmark image super-resolution by retrieving web images," *IEEE Transactions on Image Processing*, vol. 22, no. 12, pp. 4865–4878, 2013. 2
- [46] X. Yan, W. Zhao, K. Yuan, R. Zhang, Z. Li, and S. Cui, "Towards content-independent multi-reference super-resolution: Adaptive pattern matching and feature aggregation," in *European Conference on Computer Vision (ECCV)*, 2020. 2
- [47] Y. Tan, H. Zheng, Y. Zhu, X. Yuan, X. Lin, D. Brady, and L. Fang, "Crossnet++: Cross-scale large-parallax warping for reference-based super-resolution," *IEEE Transactions on Pattern Analysis and Machine Intelligence*, 2020. 2
- [48] S. Khamis, S. Fanello, C. Rhemann, A. Kowdle, J. Valentin, and S. Izadi, "Stereonet: Guided hierarchical refinement for real-time edge-aware depth prediction," in *Proceedings of the European Conference on Computer Vision (ECCV)*, 2018, pp. 573–590. 3
- [49] Z. Liang, Y. Guo, Y. Feng, W. Chen, L. Qiao, L. Zhou, J. Zhang, and H. Liu, "Stereo matching using multi-level cost volume and multi-scale feature constancy," *IEEE Transactions on Pattern Analysis and Machine Intelligence*, 2019. 3
- [50] M. Yin, Z. Yao, Y. Cao, X. Li, Z. Zhang, S. Lin, and H. Hu, "Disentangled non-local neural networks," in *European Conference on Computer Vision (ECCV)*, 2020. 4, 8
- [51] W. Shi, J. Caballero, F. Huszár, J. Totz, A. P. Aitken, R. Bishop, D. Rueckert, and Z. Wang, "Real-time single image and video super-resolution using an efficient sub-pixel convolutional neural network," in *IEEE Conference on Computer Vision and Pattern Recognition (CVPR)*, 2016, pp. 1874–1883. 4
- [52] J. Kim, J. Kwon Lee, and K. Mu Lee, "Deeply-recursive convolutional network for image super-resolution," in *IEEE Conference on Computer Vision and Pattern Recognition (CVPR)*, 2016, pp. 1637–1645. 8
- [53] Y. Tai, J. Yang, and X. Liu, "Image super-resolution via deep recursive residual network," in *IEEE Conference on Computer Vision and Pattern Recognition (CVPR)*, 2017, pp. 3147–3155. 8
- [54] W.-S. Lai, J.-B. Huang, N. Ahuja, and M.-H. Yang, "Deep laplacian pyramid networks for fast and accurate super-resolution," in *IEEE Conference on Computer Vision and Pattern Recognition (CVPR)*, 2017, pp. 624–632. 8
- [55] X. Guo, K. Yang, W. Yang, X. Wang, and H. Li, "Group-wise correlation stereo network," in *IEEE Conference on Computer Vision and Pattern Recognition (CVPR)*, 2019, pp. 3273–3282. 10, 11
- [56] N. Mayer, E. Ilg, P. Haussler, P. Fischer, D. Cremers, A. Dosovitskiy, and T. Brox, "A large dataset to train convolutional networks for disparity, optical flow, and scene flow estimation," in *IEEE Conference on Computer Vision and Pattern Recognition (CVPR)*, 2016, pp. 4040–4048. 10
- [57] R. Timofte, E. Agustsson, L. Van Gool, M.-H. Yang, and L. Zhang, "Ntire 2017 challenge on single image super-resolution: Methods and results," in *IEEE Conference on Computer Vision and Pattern Recognition Workshops (CVPRW)*, 2017, pp. 114–125. 10, 11
- [58] A. Mittal, A. K. Moorthy, and A. C. Bovik, "No-reference image quality assessment in the spatial domain," *IEEE Transactions on Image Processing*, vol. 21, no. 12, pp. 4695–4708, 2012. 11
- [59] A. Mittal, R. Soundararajan, and A. C. Bovik, "Making a "completely blind" image quality analyzer," *IEEE Signal Processing Letters*, vol. 20, no. 3, pp. 209–212, 2012. 11
- [60] J. Yan, J. Li, and X. Fu, "No-reference quality assessment of contrast-distorted images using contrast enhancement," *arXiv preprint*, 2019. 11
- [61] W. Lee, J. Lee, D. Kim, and B. Ham, "Learning with privileged information for efficient image super-resolution," in *European Conference on Computer Vision (ECCV)*, 2020. 11



Yingqian Wang received the B.E. degree in electrical engineering from Shandong University (SDU), Jinan, China, in 2016, and the M.E. degree in information and communication engineering from National University of Defense Technology (NUDT), Changsha, China, in 2018. He is currently pursuing the Ph.D. degree with the College of Electronic Science and Technology, NUDT. His research interests focus on low-level vision, particularly on light field imaging and image super-resolution.



Xinyi Ying is currently pursuing the M.E. degree with the College of Electronic Science and Technology, National University of Defense Technology (NUDT). Her research interests focus on low-level vision, particularly on image and video super-resolution.

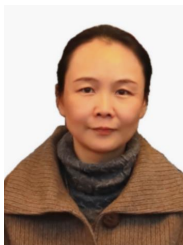


Longguang Wang received the B.E. degree in electrical engineering from Shandong University (SDU), Jinan, China, in 2015, and the M.E. degree in information and communication engineering from National University of Defense Technology (NUDT), Changsha, China, in 2017. He is currently pursuing the Ph.D. degree with the College of Electronic Science and Technology, NUDT. His research interests include low-level vision and deep learning.

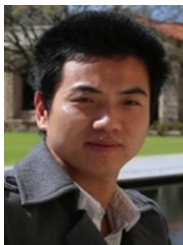


Award and the Youth Outstanding Talent of NUDT in 2016.

Jungang Yang received the B.E. and Ph.D. degrees from National University of Defense Technology (NUDT), in 2007 and 2013 respectively. He was a visiting Ph.D. student with the University of Edinburgh, Edinburgh from 2011 to 2012. He is currently an associate professor with the College of Electronic Science, NUDT. His research interests include computational imaging, image processing, compressive sensing and sparse representation. Dr. Yang received the New Scholar Award of Chinese Ministry of Education in 2012, the Youth Innovation



Wei An received the Ph.D. degree from the National University of Defense Technology (NUDT), Changsha, China, in 1999. She was a Senior Visiting Scholar with the University of Southampton, Southampton, U.K., in 2016. She is currently a Professor with the College of Electronic Science and Technology, NUDT. She has authored or co-authored over 100 journal and conference publications. Her current research interests include signal processing and image processing.



particularly on 3D feature learning, 3D modeling, 3D object recognition, and scene understanding. Dr. Guo received the ACM China SIGAI Rising Star Award in 2019, Wu-Wenjun Outstanding AI Youth Award in 2019, and the CAAI Outstanding Doctoral Dissertation Award in 2016. He served as an associate editor for IET Computer Vision and IET Image Processing, a guest editor for IEEE TPAMI, and an area chair for CVPR 2021 and ICPR 2020.

Yulan Guo is currently an associate professor. He received the B.Eng. and Ph.D. degrees from National University of Defense Technology (NUDT) in 2008 and 2015, respectively. He was a visiting Ph.D. student with the University of Western Australia from 2011 to 2014. He worked as a postdoctoral research fellow with the Institute of Computing Technology, Chinese Academy of Sciences from 2016 to 2018. He has authored over 100 articles in journals and conferences, such as the IEEE TPAMI and IJCV. His current research interests focus on 3D vision,